IOP Publishing Journal of Optics
J. Opt. **26** (2024) 093002 (17pp) https://doi.org/10.1088/2040-8986/ad5dcc

## Topical Review

# Towards subwavelength pixels: nanophotonic color routers for ultra-compact high-efficiency CMOS image sensors

**Chanhyung Park[1,5], Sangbin Lee[2,5], Taeho Lee[1], Jiwon Kang[1], Jaehyun Jeon[1], Chaejin Park[1], Sanmun Kim[1,3], Haejun Chung[2,4,*] and Min Seok Jang[1,*]**

[1] School of Electrical Engineering, Korea Advanced Institute of Science and Technology, Daejeon 34141, Republic of Korea
[2] Graduate School of Artificial Intelligence Semiconductor, Hanyang University, Seoul 04763, Republic of Korea
[3] Department of Applied Physics and Materials Science, California Institute of Technology, Pasadena, CA 91125, United States of America
[4] Department of Electronic Engineering, Hanyang University, Seoul 04763, Republic of Korea

E-mail: haejun@hanyang.ac.kr and jang.minseok@kaist.ac.kr

Received 27 March 2024, revised 17 June 2024
Accepted for publication 2 July 2024
Published 15 July 2024

**Abstract**

The proliferation of smartphones and the widespread use of camera modules necessitate complementary metal-oxide-semiconductor (CMOS) image sensors with high pixel density. The recent competitive race to miniaturize pixels has enabled commercial CMOS sensors with submicron pixels to reach sizes as small as 0.5 $\mu$m. However, further downsizing towards subwavelength pixels faces fundamental challenges as the conventional focus-and-filter approach suffers from the diminishing focusing ability of conventional microlens arrays and optical efficiency constraints imposed by absorptive color filters. Nanophotonic color routers have emerged to overcome these challenges via efficient spatio-spectral splitting, thereby directing incident light into corresponding pixels. In particular, recent developments in free-form device optimization methods enable the design of highly efficient color routers by exploring a large combinatorial design space, which was previously considered to be intractable with conventional design methods. In this review, we comprehensively introduce a multitude of research achievements in the field of nanophotonic color routers for CMOS image sensors with a special emphasis on their design methodologies.

Keywords: image sensors, color routers, color splitters, metasurfaces, inverse design, free-form optimization, adjoint method

[5] These authors contributed equally to this work.
[*] Authors to whom any correspondence should be addressed.

## 1. Introduction

The pursuit of capturing the splendor of the colorful world has been an enduring endeavor throughout human history, predominantly manifested through paintings and imaging techniques including photography. The advent of electronic color image sensors, which convert incident photons into electronic signals, was a revolutionary moment as it granted ubiquitous access to full-color photography by enabling high-resolution and compact imaging devices. These image sensors have also played a pivotal role in advancing various academic disciplines, including spectroscopy [1, 2], hyperspectral imaging [3, 4], and computer vision [5, 6]. Modern digital image sensors utilize metal-oxide-semiconductor (MOS) technology and are generally classified into two types: charge-coupled devices (CCD) and complementary MOS (CMOS) sensors. Traditionally, CCDs have dominated the image sensor market due to their low noise. However, recent advancements in CMOS image sensors over the last few decades positioned them as mainstream in the field of image sensors. In comparison to CCDs, CMOS image sensors offer advantages in terms of low power consumption, low voltage operation, on-chip integrability, and low cost [7]. Consequently, CMOS image sensors find extensive applications in high-volume products, such as smartphones and digital cameras [8].

The increasing ubiquity of smartphones and the rising deployment of camera modules on a global scale demand image sensors with high pixel density. Many global manufacturers have been engaged in this fierce race of pixel miniaturization, which ultimately enables them to integrate more pixels into the same area compared to their rivals. The early efforts have been mainly focused on improving device architecture to overcome the issues associated with pixel downscaling, namely, the reduced incident photon flux per pixel and the pixel crosstalk [9]. For example, the backside illumination (BSI) scheme was introduced to enhance pixel sensitivity by placing metal electrodes on the opposite side of the illumination [10]. Deep trench isolation and metal grid walls were incorporated to reduce electrical and optical crosstalk between neighboring pixels, respectively [11]. These endeavors have led to the popularity of commercial CMOS sensors with submicron pixels in recent years, and the state-of-the-art subpixel size has now reached 0.5 $\mu$m [12].

Further miniaturization of image sensor pixels towards subwavelength, however, requires a major breakthrough because the conventional optical components incorporated in the device start to fail as their scale approaches the diffraction limit [13, 14]. Current CMOS image sensors adopt a combination of microlens arrays (MLA) and dye-absorptive color filters to send red, green, and blue light to the corresponding subpixels, as shown in figure 1(a) [15]. As the size of each pixel becomes similar to or shorter than the wavelength of light, two critical issues jeopardize this optical scheme. First, the focusing ability of MLAs diminishes as the physics domain transitions from the ray-optics regime to the wave-optics regime [16]. Second, more fundamentally, absorptive color filters simply dissipate the unwanted spectral ranges of incident light and thereby impose limits on optical efficiency. Consequently, a Bayer filter constrains the maximum optical efficiency of R, G, and B pixels to be 25%, 50%, and 25%, as schematically illustrated in figure 1(a). As the physical area of a pixel reduces, the photon influx per pixel reduces proportionally. Therefore, this imposed limit on optical efficiency becomes a critical obstacle to pixel downscaling.

To overcome these issues, new types of optical devices have been extensively investigated to replace conventional microlens and absorptive color filters. These new devices, called nanophotonic color splitters or color routers, are designed to function in the wave-optic regime and spectrally split and direct incident light into corresponding pixels, as shown in figure 1(b), eliminating the efficiency bound imposed by dissipative filters. This attempt was inspired by recent developments in meta-optics technology, which have significantly facilitated the development of such nanophotonic imaging devices. In this scheme, attributes such as sub-wavelength capabilities [17, 18], expansive color gamut coverage [19, 20], and inverse-design devices [21, 22] have garnered attention for their efficacy in spectrum selection and digitization. Additionally, the slim profiles of these devices, compared to conventional counterparts, contribute to their suitability for integrated cameras in next-generation vision systems. The use of advanced optimization methods for highly combinatorial device design problems [23], such as genetic algorithms (GA) [24–26] and adjoint methods [27–29], further empowers the development of free-form nanophotonic color routers for CMOS image sensors.

This Review provides an in-depth overview of a multitude of research achievements in the field of nanophotonic color routers for CMOS image sensors. Although some previous review articles comprehensively introduced this emerging field [30–32], the rapid development of free-form device design methods has created a new paradigm for nanophotonic color routers, necessitating a more focused review with a special emphasis on their design methodologies. This Review is structured as follows. In the next section, we introduce fixed-form nanophotonic color splitters utilizing distinct physical phenomena including diffraction, plasmonic and dielectric resonance, and geometric and propagational phases. These fixed-form devices adopt relatively simple device structures based on primitive shapes chosen based on physical intuition. Low degrees of design freedom make it relatively easy to optimize these devices but often constrain their expected optical performance. On the other hand, free-form color routers, which we discuss in section 3, tend to possess much higher performance but are difficult to optimize due to their huge design complexity that grows exponentially with the degrees of freedom. We provide an in-depth introduction to the two major design methodologies for free-form device design: GA and adjoint variable methods. Finally, we discuss the remaining challenges in the field of nanophotonic color routers to ensure their application in advanced CMOS image sensors. We also provide two summary tables that outline the advantages and challenges of various design methods for nanophotonic color routers (table 1) and systematically compare previously proposed devices discussed in this review (table 2).

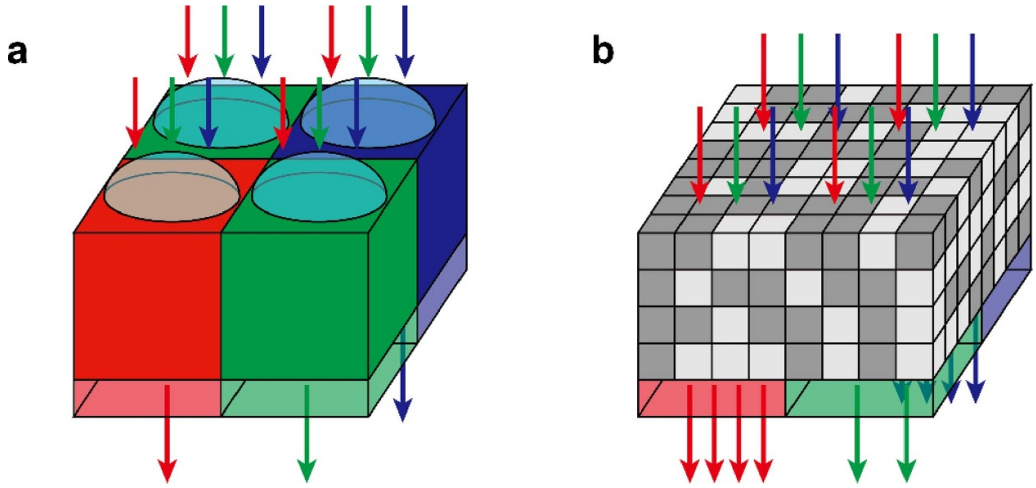


**Figure 1.** Comparison between conventional CMOS image sensor (a) and free-form nanophotonic color router (b) design schemes. In conventional designs, CMOS image sensors focus the incident light with microlens arrays and filters with dye-absorptive filters. Due to the color filters, the maximum color routing efficiency is limited. In contrast, a free-form design scheme allows for perfect routing of incident light through non-trivial shapes and topology modifications.

**Table 1.** The physical principles and optimization methods utilized in nanophotonic color router design including their advantages and challenges.

| Principle/Optimization Method | | Advantages | Challenges |
|---|---|---|---|
| Fixed-form | Plasmonic resonance | Highly localized optical response → high spatial resolution and insensitive to the incidence angle | Limited optical efficiency due to high ohmic dissipation |
| | Dielectric resonance | Negligible ohmic dissipation | Limited spatial resolution due to diffraction limit |
| | Geometric phase | Required phase delay directly translates to meta-element orientation | Only works for circular polarization |
| | Propagation phase | Relatively high optical efficiencies | Meta-elements require large vertical aspect ratio |
| Free-form | Genetic algorithm | Easy implementation | Difficult to handle large degrees of design freedom (>1000) → limited color routing efficiency |
| | Adjoint method Automatic differentiation | Can handle large degrees of freedom → near-perfect theoretical routing efficiencies achieved | Designed device structures are often too complex to fabricate |

## 2. Fixed-form color routers

With a deeper understanding of nanophotonics and advances in fabrication techniques, devices with a spectral response similar to that of a conventional CMOS image sensor have emerged. The earliest works focused on designing transmissive color filters that could potentially replace conventional dye-based color filters and are yet compatible with a higher pixel resolution. The nanophotonic color filters can be achieved by utilizing local optical resonances. Yokogawa *et al* demonstrated color filters based on plasmonic hole arrays which maintain their filtering function down to 1 $\mu$m pixel pitch [47] and Berzinš *et al* employed high-index dielectric resonances based on silicon nanopillars to achieve submicron color filtration [48].

However, the major limitation of this alternative color 'filter' approach is that the light entering the undesired color region is completely excluded. Even if a perfect color filter with 100% efficiency is developed, only 25% of the total incident red and blue light and 50% of the green light can be utilized as depicted in figure 1(a). Therefore, an alternative color 'routing' approach is proposed to sort R, G, and B light to the desired color region pixels as schematically shown in figure 1(b). This kind of approach has the potential to significantly outperform previous works, which led to the development of various works, demonstrating huge performance improvement and technical progress.

The initial implementation of nanophotonic color routers was conducted based on physics-inspired fixed-form design approaches, where devices are composed of optical elements of simple primitive shapes such as rectangles and cylinders that are chosen based on physical intuitions. Design optimizations of these devices were performed by varying only the structural parameters such as length, height, or radius of

**Table 2.** The physical principle and optimization method, type, pixel pitch, degree of freedom, materials, incident beam polarization, and color routing efficiencies of the various color routers.

| Principle/Optimization Method | | Pixel Pitch ($\mu$m) | Type | Materials | Degree of freedom (Free-form only) | Polarization | Color routing efficiency (peak) | References |
|---|---|---|---|---|---|---|---|---|
| Fixed-form | Dielectric scattering | 1.43 | 1D RGB | SiN | | Polarization-independent | 40%–50% (experiment) | [33] |
| | Dielectric scattering | 1 | 2D RGB-NIR | $Si_3N_4$ | | Polarization-independent | 63% (experiment) | [34] |
| | Geometric phase | 25 | 2D Bayer RGB | GaN | | Circularly polarized input | 30% (experiment) | [35] |
| | Propagation phase | 0.84 | 2D Bayer RGB | SiN | | Polarization-independent | 51% (experiment) | [36] |
| Free-form | Genetic algorithm | 1.1 | 1D RGB | Air, $TiO_2$ | 33 × 11 | TE polarized input | >50% (simulation) | [37] |
| | Genetic algorithm | 1 | 2D Bayer RGB | Air, $Si_3N_4$ | 16 × 16 | Polarization-independent | 55.3% (experiment) | [38] |
| | Genetic algorithm | 0.8 | 2D Bayer RGB | Air, $TiO_2$ | 20 × 20 | Polarization-independent | 60.2% (experiment) | [39] |
| | Genetic algorithm | 0.25 | 1D RGB | Refractive indices (1.5, 2) | 32 × 4 | TE and TM responses averaged | 68.2% (simulation) | [40] |
| | Adjoint method | 1 | 2D Bayer RGB | $SiO_2$, $TiO_2$ | 100 × 100 × 100 | Polarization-dependent sorting | 77% (simulation)<br>57% (experiment)[a] | [41] |
| | Adjoint method | 15.075 (3.3 $\lambda_{mid}$)[b] | 2D | Air, IP-Dip polymer | 40 × 40 × 6 | Polarization-dependent sorting | 71.7% (simulation)<br>46.7% (experiment)[b] | [42] |
| | Adjoint method | 0.4 | 1D RGB-IR | $SiO_2$, $Si_3N_4$ (grayscale) | 160 × 200 | TM polarized input | >99% (simulation) | [43] |
| | Adjoint method | 0.32 | 2D Bayer RGB | $SiO_2$, $TiO_2$ (grayscale) | 64 × 64 × 50 | Polarization-independent | >98% (simulation) | [44] |
| | Adjoint method | 0.33 (6 wavs), 0.99 (9 wavs) | 2D spectral 6, 9 wavs | $SiO_2$, $TiO_2$ (grayscale) | 33 × 33 × 50 | Polarization-independent | >98% (simulation) | [45] |
| | Automatic differentiation | 0.6 | 2D Bayer RGB | Air, SiN | Unspecified [c] | Polarization-independent | 60.7% (simulation)<br>42.3% (experiment) | [46] |

[a] The experiment was performed based on the same methodology but in the microwave regime operating in the $K_a$ band (26–40 GHz), scaling up by a factor of ×17 500.
[b] The experiment was performed in the mid-infrared wavelengths, which has a center wavelength of 4.35 $\mu$m.
[c] The minimum feature size of the device is 50 nm.

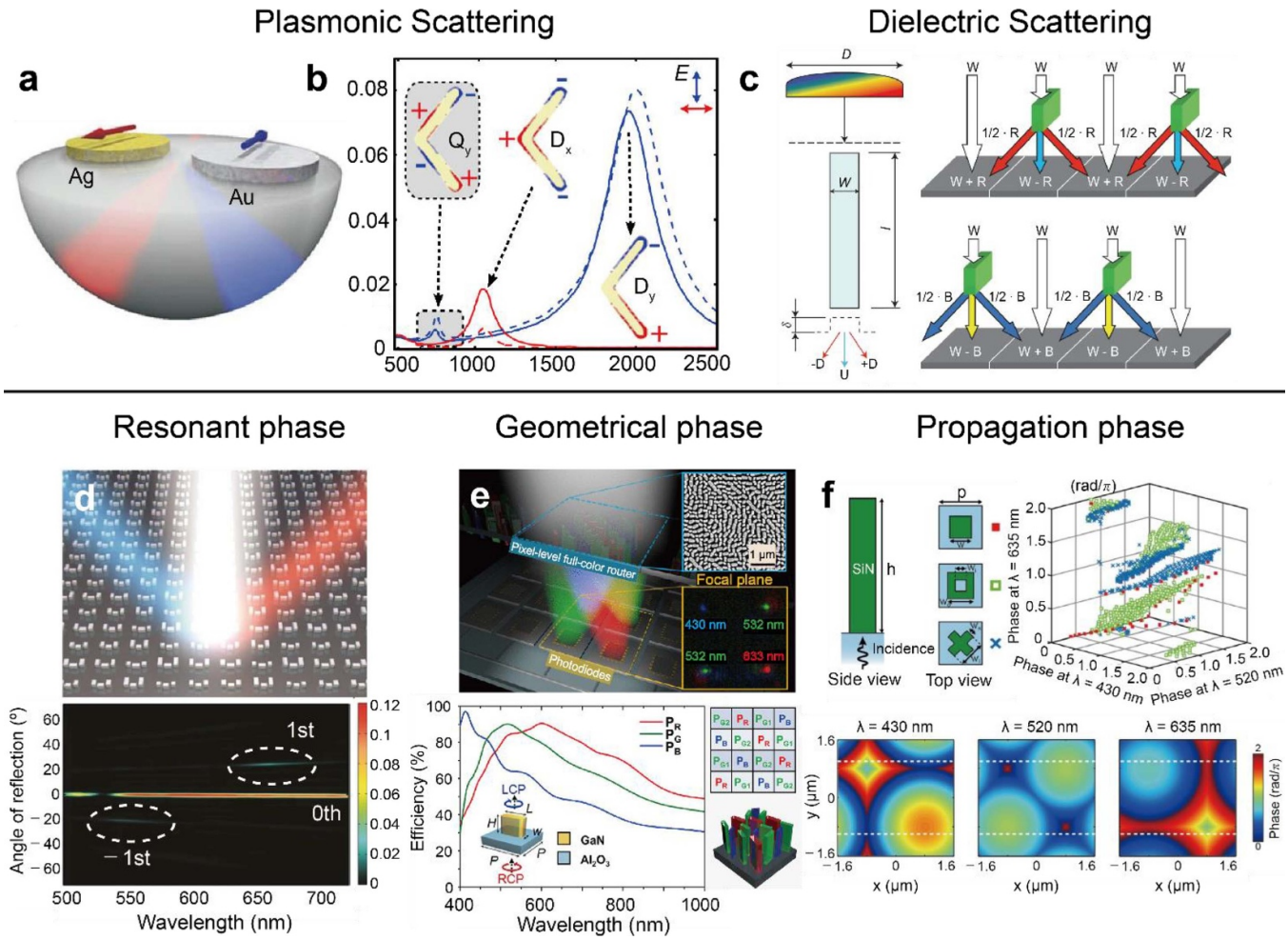


**Figure 2.** Fixed-form color routers. (a) Plasmonic color router based on asymmetric coupled Ag and Au dimers. Reproduced from [49], with permission from Springer Nature. (b) Plasmonic color router based on a single V-shaped nanoantenna. Reprinted with permission from [50]. Copyright (2013) American Chemical Society. (c) Schematic of a color-splitting configuration with a dielectric scatterer. Reproduced from [51], with permission from Springer Nature. (d) Schematic of a color router with multi-resonator metasurfaces based on Fano resonance. Reproduced from [52], with permission from Springer Nature. (e) GaN Bayer pattern color router based on geometrical phase. Reprinted with permission from [35]. Copyright (2017) American Chemical Society. (f) Schematic of a metasurface color router based on propagation phase and the phase library of the SiN nanopillar. Reproduced from [36]. CC BY 4.0.

the elements while the shape of the elements remained fixed. Since the fixed-form devices typically involve only a small number of design degrees of freedom (<5), their structure could be readily optimized via simple optimization methods or even with brute force parameter sweep. The small number of design parameters, however, also generally results in constrained device performance as a large portion of the potential design space remains unexplored [23].

Various physical principles have been employed to spatio-spectrally split and route incident broadband light. In order to direct light in desired directions depending on their wavelength with a high spatial resolution, subwavelength metallic scatterers were initially investigated. Metal nanostructures support plasmonic resonances at different wavelengths depending not only on their material composition but also on their sizes and shapes [53]. One can utilize these multiple plasmonic resonances in a subwavelength metallic structure to induce wavelength-dependent scattering patterns that can be engineered to split colors of incident light. As a notable example, Shegai *et al* demonstrated that a pair of closely spaced Au and Ag nanodisks, illustrated in figure 2(a), asymmetrically scatters light toward Ag nanoparticle side for the wavelength below 500 nm (∼blue), but the direction of scattering shifts toward Au particle side for the wavelength longer than 500 nm (∼red) regardless whether the incident light is polarized parallel or perpendicular to the dimer axis [49]. For dimer-perpendicular polarization, the directivity reaches +7 dB at around 450 nm and −12 dB at around 680 nm. This switching behavior can be explained by the interplay between material-dependent plasmon resonances of composing Au and Au nanoparticles. We note that color routing is still achievable even with a nanostructure composed of a single metal as long as the structure can support multiple plasmonic resonances [50, 54, 55]. For example, a V-shaped nanoantenna supports multiple resonances, as illustrated in figure 2(b), and exhibits a maximum directivity of 15 dB at a wavelength of 800 nm, with a V-shaped nanoantenna having a 120° opening angle [50]. A single V-shaped

nanoantenna possesses three strong localized plasmonic resonances in the target spectrum; A $x$-polarized fundamental dipole mode $D_x$, $y$-polarized dipole $D_y$, and quadrupole $Q_y$. modes. These modes are spectrally overlapped and interfere with each other to produce asymmetric radiative patterns depending on wavelength. Similar bidirectional functionality was achieved for dielectric V-shaped nanoantennas [55]. A long Ag nanorod can also route colors based on longitudinal multipolar resonances [54]. Plasmonic nanostructures can also offer subwavelength color sorting capability through on-chip integration with photodetectors. Kim *et al* demonstrated that a binary grating composed of poly-Si trenches with different widths on an Ag film sorts the red and blue photons into their respective trenches by leveraging anti-Hermitian coupling between resonant photodetector elements [56]. This device exhibited near-unity color-sorting efficiencies with a narrow spectral response of ∼30 nm linewidth and a subwavelength grating period that can be effectively translated into a sub-pixel size of ∼100 nm.

To avoid ohmic dissipation in plasmonic scatterers, nanophotonic scatterers based on dielectrics have also been investigated for color routing. It has been known that the scattering patterns of a dielectric particle can be precisely tailored by altering the shape of the particle [57]. Nishiwaki *et al* proposed SiN deflectors to split colors into multiple directions and demonstrated their color sorting capability through integration with high-pixel-density image sensors [51]. The proposed light deflector has a simple plate-like structure as shown in figure 2(c). When light vertically impinges the deflector, it accumulates a phase difference along the long axis of the deflector due to the index difference between the deflector and the surroundings. When the accumulated phase difference across the deflector is an even multiple of π, the transmitted light propagates forward. On the other hand, when the phase difference becomes an odd multiple of π, forward radiation is suppressed and symmetric side lobes appear. Since the phase accumulation depends on the wavelength of incident light, it is possible to realize color-specific light deflection. By placing one-dimensional red and blue deflector arrays in an alternating manner as illustrated in figure 2(c), a Bayer-like two-dimensional color pattern can be accomplished. By integrating this color router array on conventional CCDs with 1.43 $\mu$m pixels, the authors experimentally confirmed that this color router effectively separates colors by delivering 1.85 times more light to the photodetectors compared to conventional absorptive color filters. Based on a similar principle, Miyata *et al* from NTT Corporation designed a CMOS process-compatible color splitter [33]. In this work, dielectric nanoposts of various widths were employed to generate desired phase differences. The proposed color splitters consist of two different sizes of nanoposts that provide phase gradients along different directions for red, green, and blue light. Shao *et al* improved the routing efficiency of a near-infrared (NIR)-RGB CMOS-compatible spectral router with a similar methodology while reducing the pixel pitch to 1 $\mu$m [34]. Based on the particle swarm optimization algorithm combined with finite-difference time-domain (FDTD) simulations, the optimized color routing efficiency of the designed routers with color filters has reached to 63%.

Nanophotonic local phase modulation can also be leveraged to create metasurfaces that enable more elaborate wavefront shaping with a subwavelength resolution [58]. By mimicking the phase profile of conventional large-scale optical structures, metasurfaces have demonstrated some remarkable achievements in optical applications, such as beam deflectors [59–61], metalens [62–65], quarter-wave plates [66, 67], and holograms [68–70]. Notably, achieving an achromatic response is one of the important properties of designing metasurfaces in these applications, especially in metalens design. Reversely, if a metasurface is designed to enhance chromatic aberration, it effectively functions as a color-splitting device.

The mechanisms of local phase modulation in metasurfaces can be divided into three categories: resonant phase, geometric phase, and propagation phase [58, 71]. We note that both plasmonic and dielectric metasurfaces can utilize resonance and geometric phases, but the propagation phase is only effective in dielectric metasurfaces because propagation of surface plasmons generally involves significant optical loss. Fixed-form metasurfaces are designed based on subwavelength unit cells called meta-atoms possessing simple primitive shapes such as rectangles and cylinders. By placing meta-atoms with appropriate phase dispersions, one can achieve desired spatio-spectral phase distributions with subwavelength spatial resolution. The resonance phase modulation is based on local optical resonances in meta-atoms. Yan *et al* devised a metasurface color splitter based on plasmonic Fano resonances in Ag-based nanostructures [52]. By imposing a linearly slanted phase gradient only for a specific wavelength, this metasurface reflects most of the incident light in a specular manner but deflects the specific wavelength to a higher-order diffraction channel. Here, the wavelength-dependent phase gradient was obtained by periodically arranged supercells consisting of four meta-atoms having slightly shifted resonance wavelengths. The phase of the plasmonic resonance varies abruptly as the resonance wavelength of the meta-atoms shifts across the target wavelength. Each meta-atom was composed of three Au nanorods: a center nanorod having a fixed length perpendicular to the grating direction and a pair of parallel nanorods along the grating direction as shown in figure 2(d). The required shift in resonance wavelength is obtained by altering the length of the pair of parallel nanorods. In a single band operation at $\lambda_0 = 750$ nm, the color routing efficiency reached up to 81%. For dual-band operation in the visible spectrum, the authors incorporated two different types of supercells in a grating period, demonstrating clear −1st and 1st order diffractions at $\lambda_0 = 532$ nm and 660 nm, respectively, as shown in the bottom panel in figure 2(d). However, the measured routing efficiency for each color channel was significantly compromised down to 5%. For small dielectric nanoparticles, overlapping of electric and magnetic dipole moments can generate the directivity between forward and backward scattering, called the Kerker effect [72]. As the size of the nanoparticles increases, multiple modes are involved in the scattering process, enabling elaborate tailoring of the scattering direction in the spatial domain [73, 74]. Yan *et al* designed a color router based on a generative

adversarial network (GAN) for both axial and lateral scattering that enables 180-degree scattering. The AI-generator designed Si structures that exhibit targeted wavelength-dependent radiation angles, which are capable of RGB color routing [75].

The geometric phase, also known as the Pancharatnam-Berry phase [76], is a polarization-sensitive phase acquired due to the orientation of anisotropic antennas, offering a convenient and robust route for broadband phase modulation. Since the geometric phase is proportional to the orientation angle of a meta-atom, one can easily implement complicated wavefronts by simply adjusting the local orientations of meta-atoms [70, 77, 78]. One of the easiest ways to to design a metasurface color router is to segmentize multiple metalenses with different focal points and operating wavelengths, and then mix them up into a single structure [79–82]. For example, three metalens working at RGB colors can be mixed into a single circular lens [79]. The mixed multifunctional metalens with a diameter of 96 $\mu$m splits 480, 550, and 620 nm light with a focal length of 100 $\mu$m, while the focal points are separated in the focal plane by 10 $\mu$m. They implemented the multifunctional metalens and found that the three colors are separated clearly. However, due to its shape and size, it is not applicable to CMOS image sensors with pixels. Therefore, a CMOS-compatible gallium nitride (GaN) pixel-level full-color router was demonstrated [35]. In this work, GaN nanopillars on an $Al_2O_3$ substrate were optimized to maximize the right-hand circular-polarization to left-hand circular-polarization conversion efficiency at R, G, and B colors, as shown in figure 2(e). The optimized nanopillars were strategically positioned to focus their respective colors in the Bayer pattern, guided by geometric phase calculation. Measured optical efficiencies of the optimized color router of R, G1, B, and G2 were 15.9%, 37.86%, 38.33%, and 27.56%, respectively, with a square dimension of 50 $\mu$m $\times$ 50 $\mu$m, and focal length of 110 $\mu$m. It is far from the extremely high optical efficiency of individual GaN-based metalenses, which is 87%, 91.6%, and 50.6% for blue, green, and red light, respectively. This discrepancy can be explained by optical crosstalk and the reduction of the effective area within the color router. However, this result is meaningful since it is comparable to the conventional CMOS image sensors. We also note that there are some existing works, such as a clear hologram image that represents a rose flower [83], and an aluminum nitride color router working at UV range [84], which are designed with a similar methodology.

Many of the previously described metasurface color routers were composed by integrating three different types of meta-atoms, each of which is active only for a specific color. Therefore, the effective metasurface area per color was only a fraction of the whole metasurface area, making it difficult to achieve high-efficiency color routing. To overcome this issue, it is required to make meta-atoms active for all colors by fulfilling all wavelength-dependent phase conditions simultaneously. However, simple cuboid structures adopted in most of the early works often fail to provide sufficient phase-dispersion coverage to ensure color router operation. To overcome this issue, one can increase the structural complexity of a unit cell to secure enough degrees of freedom to cover a larger portion of the phase-dispersion space, either by diversifying the shape of the nanoposts [36, 85–87] or by stacking multiple layers vertically [88, 89] to increase the structural complexity of a unit cell.

Miyata *et al* from NTT Corporation employed three different types of 1250 nm-high SiN nanoposts—filled square, square frame, and X-shape—as depicted in figure 2(f) for propagation phase modulation [36]. By altering the dimensions of these various shapes nanoposts, the authors were able to access a sufficient portion of the phase-dispersion space to generate different transmission phase distributions for $\lambda_0 = 430$, 520, and 635 nm shown in the bottom panel of figure 2(f) that focus blue, red, and green light to corresponding pixel positions, respectively. The spatial resolution of phase distributions is determined by the size of a unit cell. By choosing the nanopost period of 280 nm, the authors were able to successfully demonstrate the operation of the metasurface color router combined with 0.84 $\mu$m pixel image sensors. The measured average sorting efficiency and acceptance angle were 51% and 16.5°, respectively. Several other studies have used similar principles to design NIR-visible color routers [86, 87].

More recently, researchers from Samsung began to fabricate 0.56 $\mu$m pixel CMOS image sensors based on the propagation phase difference [90]. By using high refractive index $TiO_2$ nanoposts embedded in a low refractive index medium, it became possible to design a condition that simultaneously satisfies the desired phase distribution for each representative wavelength. The proposed structure showed clear color-routing functionality. Moreover, with the integration of a commercial 0.8 $\mu$m Bayer image sensor, the newly designed structure showed that it can substitute MLA by exhibiting higher luminance. Samsung also demonstrated a two-layered nano-prism structure for a high-sensitivity 0.64 $\mu$m pixel CMOS image sensor that is superior to the same image sensor with a conventional MLA [91].

Mansoree *et al* demonstrated a 2.5D metastructure composed of two metasurface layers introduced to split 780 and 915 nm normally incident light into different focal points [88]. They first calculated spatially varying phase profiles for two different wavelengths and placed meta-atom that best suited the desired phase profiles. Next, they performed an adjoint method to optimize focal spot intensities for the two wavelengths by giving adjoint sources as the surface electric current densities. The two differently optimized structures showed different optical efficiencies. Device optimization using the phase dispersion library resulted in focusing efficiencies of 33% and 29% at wavelengths 780 and 915 nm, respectively. They are significantly lower than those predicted by the direct design model, which are 86% and 88%. This large discrepancy indicates that the assumption that the amplitude and phase of the designed unit cell in an optimized color router are the same as that of the same unit cell in a periodic condition fails. The optimized device based on the adjoint method showed better simulated focusing efficiencies of 52% and 49%, exploiting the fascinating power performance of the adjoint method.

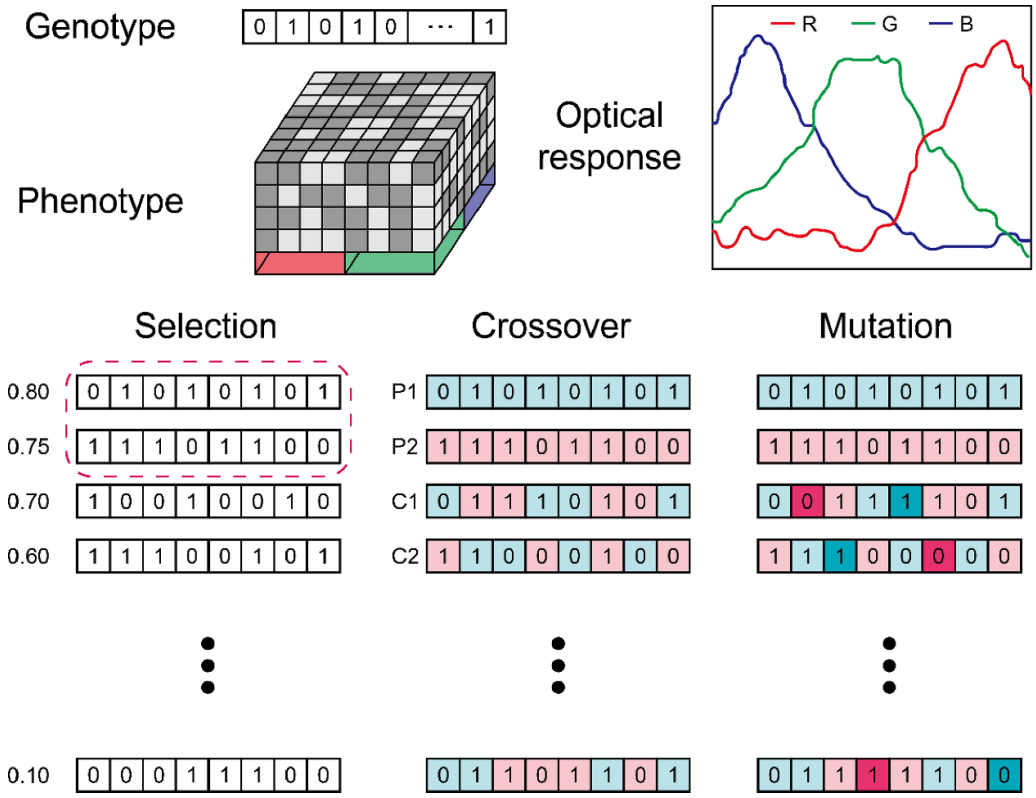


**Figure 3.** Schematic of the optimization process of a free-form color router using the genetic algorithm. The design space is divided into multiple unit cells and represented as genotypes. Based on the electromagnetic simulations, the optical efficiency is calculated to determine the performance of the genotypes. Selection, crossover, and mutation are the three components of optimization.

## 3. Free-form nanophotonic color routers

The nanophotonic color routers described above are designed by a fixed-form approach. In this design scheme, optical devices are composed of simple-shaped elements chosen by physical intuitions and only the dimensions of the elements are tuned during the device optimization while their shapes remain fixed. Since this design approach only considers a constrained set of structures, a large portion of design potential has remained unexplored. However, advancements in computational power and electromagnetic simulations, along with optimization methods, have enabled the numerical optimization of structures with complex geometries and relatively large design parameters that were previously inaccessible. Consequently, many researchers have directed their attention to the free-form design approach, which allows the elements of a nanophotonic device to have non-trivial shapes and both the shape and the topology of the structure can be freely revised during the device optimization [23]. This approach grants access to significantly greater design space and is thus likely to produce better-performing device structures compared to the traditional fixed-form approach. Since free-from structures involve a large number of design parameters (>100), their combinatorial design space, which grows exponentially with the degrees of design freedom, easily exceeds the number of atoms in the universe ($\sim 10^{80}$) [23, 92]. To handle such a large design space, researchers have devised a variety of numerical optimization methods spanning from classical optimization heuristics to machine learning techniques [23, 59, 60, 93]. In this review, we focus on two most popular design methods: the genetic algorithm and the adjoint-based method. In this Section, we provide an introduction to each method and discuss associated free-form nanophotonic color routers.

### 3.1. Genetic algorhtim

Genetic algorithm (GA) is a widely used optimization algorithm in a variety of fields, including economics, engineering, politics, and management [94]. Mimicking the evolutionary processes found in nature, GA considers each design parameter as a gene, forming a small ecosystem with various parameter genes. Here, the list of design parameters is called genotype and the actual device structure associated with the gene is called phenotype as illustrated in figure 3. The optimal gene is identified through iterative evolution. Throughout this process, three operations—selection, crossover, and mutation—are performed. The whole process of evolution is schematically described in figure 3. During the selection process, genes that demonstrate high performance in the current ecosystem are chosen. A crossover takes place between two genes that survive the selection process. In this step, the two genes become the parents, and their respective genes are combined or interchanged to generate new children. Mutation occurs after the crossover operation and randomly perturbs the design parameter values. This randomization helps the population to get

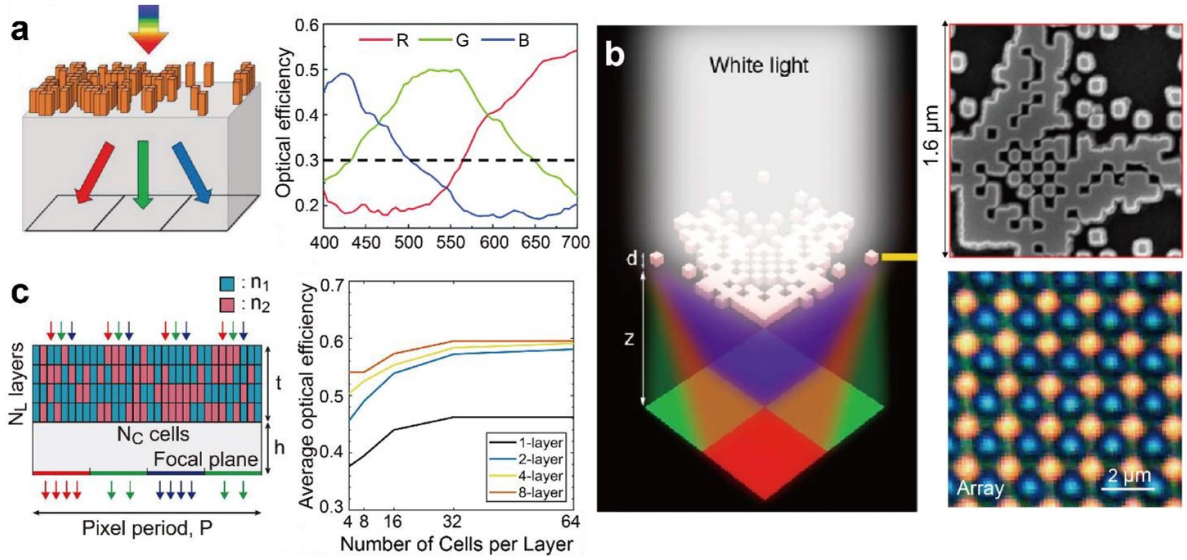


**Figure 4.** Free-form nanophotonic color routers based on genetic algorithms. (a) A QR code-like single-layer RGB color router and its spectral responses. Reproduced from [37] with permission from the Royal Society of Chemistry. (b) A schematic and the SEM image of the single layer Bayer pattern color router and the experimental color image. Reprinted with permission from [39]. Copyright (2022) American Chemical Society. (c) A schematic of a multi-layer nanophotonic color router and the dependence on optical efficiency with design parameters. Reprinted from [40], Copyright (2023), with permission from Elsevier.

out of local extrema [95]. Since GA is a long-standing and easily implementable optimization technique, numerous works in the field of nanophotonics adopted GA as an optimization method. Those devices include broadband absorbers [96–98], light trapping devices [26], beam deflectors [25, 99, 100], and metalens [100–102].

Evolutionary algorithms including GA have been frequently employed in designing color routing devices [37–40, 103, 104]. Most of these works adopt explicit grid representations, where the design space is divided into $N = N_1 \times N_2$ rectangular grids, and each grid node can be either filled with a material or empty. Naturally, the genotype of a device is a binary array having $N$ elements, which makes the optimization problem a binary combinatorial problem. Chen *et al* theoretically designed a free-form color router made of titanium oxide as shown in figure 4(a) [37]. The 1.1 $\mu$m $\times$ 1.1 $\mu$m design region was divided into 100 nm $\times$ 100 nm binary cells (i.e. 11 $\times$ 11 grids) and optimization was performed using GA. The designed color router is predicted to have peak color sorting efficiencies higher than 50% as shown in the right panel of figure 4(a), which far exceeds the upper bound of the conventional absorptive color filters, 33%, for 1D RGB pixel configuration. Interestingly, the authors showed the supremacy of their free-form design approach over other conventional metasurface design methods based on the propagation phase, geometric phase, and resonance phase by making a direct comparison of the resulting device performances.

The improved color sorting performances of GA-designed free-form color routers have also been experimentally verified in the following works [38, 39, 103]. Zou *et al* designed a 1 $\mu$m $\times$ 1 $\mu$m pixel single-layer Bayer-type free-form meta color router with 16 $\times$ 16 nanopillars [38]. Each unit cell is assigned to either silicon nitride or air with a pillar height of 600 nm. A diagonal symmetry was imposed to remove the polarization dependence of the designed color router. The designed color router was fabricated on a 500 $\mu$m thick quartz glass substrate. The measured peak optical efficiencies were 58, 59, and 49% for R, G, and B normally incident light, respectively. The optimized structure exhibited strong robustness to off-angle incidence, maintaining high color imaging quality up to an incident angle of 11°. Around the same time, Li *et al* fabricated a free-form meta color color router with a pixel pitch of 0.8 $\mu$m $\times$ 0.8 $\mu$m [39]. In contrast to prior research, this work utilized titanium oxide and air as material components to increase the refractive index contrast, and the design grid resolution was increased to 20 $\times$ 20 as shown in figure 4(b). As shown in the SEM image in the upper-right panel of figure 4(b), the structure of the color router was designed to be diagonally symmetric, which reduces the size of the design space and guarantees polarization-independent optical responses. The measured average optical efficiency of the fabricated device was 48.5%, which agrees well with the theoretical value of 49.6% displaying a clear RGB Bayer image pattern as illustrated in the below-right panel of figure 4(b). This device also showed its validity up to an off-normal incident angle of 5°.

Despite the increasing interest in color routers, there has not been any systematic investigation into the choice of device design parameters such as the device dimensions, the selection of materials, and the degrees of design freedom, which have a critical effect on the performance of a device. Due to the lack of systematic investigations, the choice of such parameters in the previously reported works was based on simple deductions such as Fabry–Perot resonance conditions or even worse, based on the computational resource availability. Kim *et al* investigated the effect of such design parameters on the

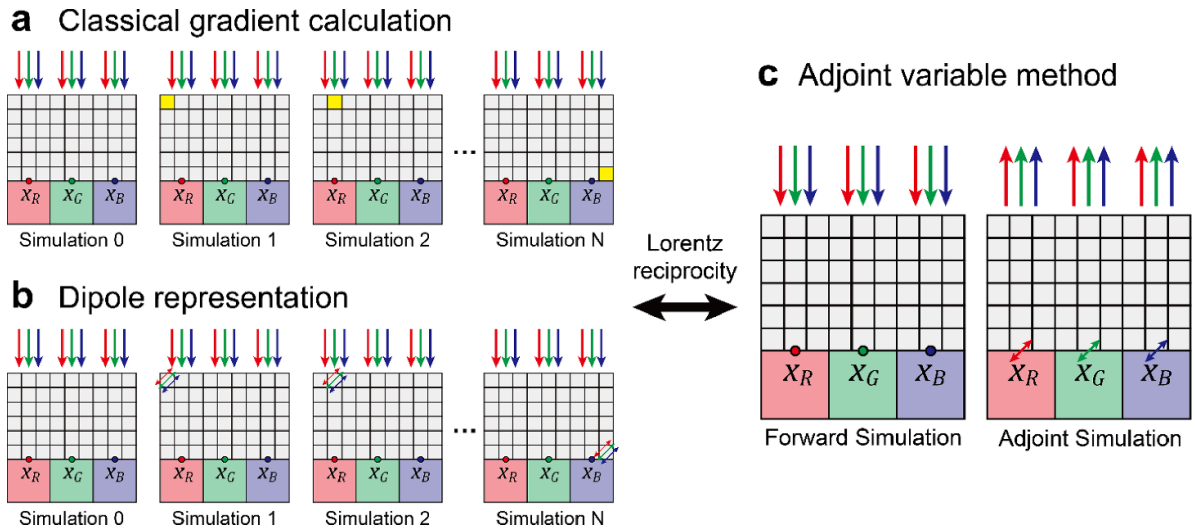


**Figure 5.** Schematic of the optimization process of a free-form color router using the adjoint method [105].(a) Illustration of the brute force approach, where all possible changes in design parameters are calculated to maximize the FoM. (b) Representation of a method for approximating minor variations in the electric field caused by incident waves and scattering objects as point-source radiation via dipole moments on a grid of N design regions. (c) Depiction of the reduction of N simulations to a single adjoint simulation by redefining electrical connections between the grid of designable regions and the target field through Lorentz reciprocity. This refinement enables the effective focusing of RGB light on each pixel through two simulations: one forward and one adjoint.

optical efficiency of the optimized color router by performing a large number of GA-based structural optimizations for a variety of design parameter choices [40] (figure 4(c)). In their work, the design parameters are characterized into two categories: physical parameters and the degrees of design freedom. The physical parameters include the period and thickness of the color router, focal length, and the refractive indices of the dielectric components. The degrees of design freedom include the number of grid layers and the grid elements in a layer. For a 1D color pattern, it was demonstrated that the pixel pitch can be decreased down to 0.25 $\mu$m without a significant efficiency loss. The reported peak color routing efficiency for this pixel pitch is 68.2%. Notably, they showed that there exist optimal refractive index pairs, and the optical efficiency drops when the refractive index contrast becomes greater than the optical value, unlike the case of metalens. They also emphasized that the number of layers plays a pivotal role in determining the device's performance as shown in the right panel of figure 4(c).

### 3.2. *Adjoint method*

As discussed in the previous subsection, GA and other population-based global optimizations effectively design and optimize free-form color routers with modest degrees of freedom ($<10^3$). However, if the given design problem becomes more complicated with DoF exceeding a few thousand, global optimization becomes impractical due to the required computational power. In this case, considering gradient-based optimization methods would be a viable option. For design problems with high DoF, an efficient calculation of the gradients is crucial. The brute force method is one of the ways of calculating gradients, as illustrated in figure 5(a). This method obtains the gradient of FoM with respect to the change of the design parameters by performing a simulation of a device with the design parameter slightly modified from its original value, which is highlighted in yellow in figure 5(a), and taking the difference between the FoMs of the simulations before and after the modification of the design parameters. As a result, the number of required simulations to calculate a FoM gradient scales linearly with the number of grid cells in the device, making it inefficient for optimizing devices with high spatial DoF. Therefore, employing an efficient method of computing gradient values for design problems with a high DoF is essential.

The adjoint method, large-scale computational optimization, provides a possible solution to overcome the computational burden in brute force optimization. The adjoint optimization allows obtaining the gradient with respect to the change of design parameters through only two simulations regardless of the number of DoF by leveraging the Born approximation [106] and Lorentz reciprocity [107]. The Born approximation assumes that induced electric dipoles in molecules or atoms determine the small response of the system to the electric field. This approximation allows for a straightforward calculation of the electric dipole moment, representing the system's response to the electric field. Using the Born approximation, one can approximate the magnitude of the induced electric field at each grid point as an electric dipole moment, as schematically shown in figure 5(b). According to Lorentz reciprocity, the relationship between an oscillating dipolar source and the resulting electromagnetic field remains constant even if the positions of the source and the measurement point are exchanged [107]. Consequently, the electromagnetic field at a point of measurement, induced by variations in material permittivity, is equivalent to the field at a perturbed point caused by a source at the measurement location, as illustrated in figure 5(c). Hence, the implementation of an 'adjoint' simulation allows for the assessment of the permittivities variation impact across the

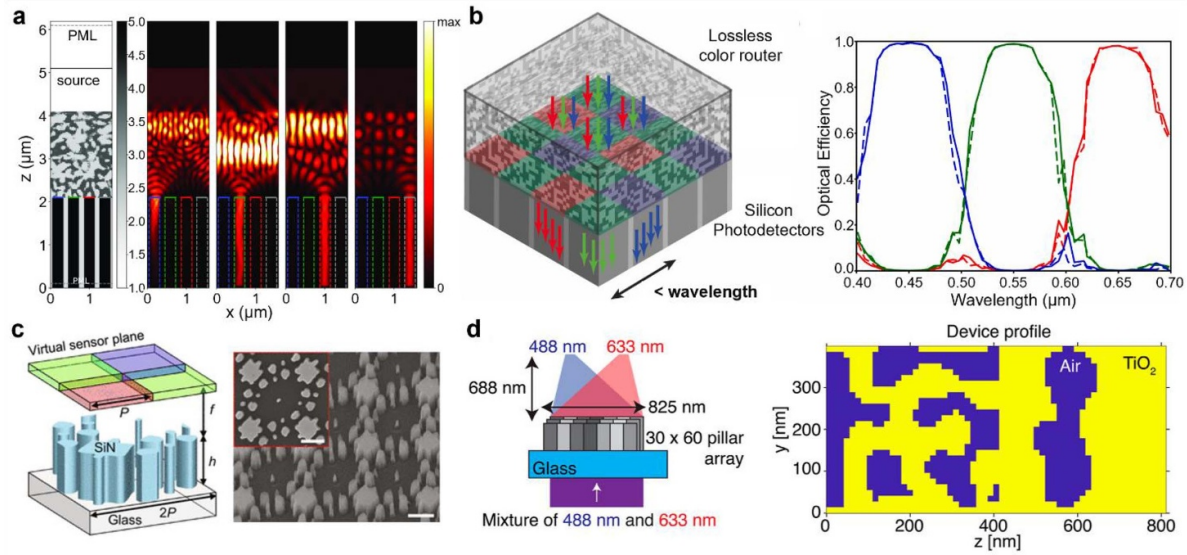


**Figure 6.** Free-form nanophotonic color routers based on adjoint method and automatic differentiation. (a) Perfect spectral routing in an RGB-IR array configuration based on adjoint method [43]. John Wiley & Sons. © 2021 The Authors. Advanced Photonics Research published by Wiley-VCH GmbH. (b) Perfect Bayer pattern nanophotonic color router based on adjoint method and the spectral responses. Reproduced from [44]. CC BY 4.0. (c) A schematic and SEM images of a free-form polarization-sensitive single layer nanophotonic color router based on the automatic differentiation of RCWA. Reproduced with permission from [46]. CC BY-NC 4.0. (d) A schematic and the designed free-form color router based on a time-reversal differentiation of FDTD. Reprinted with permission from [114]. Copyright © 2023 American Chemical Society.

entire design space with merely two simulations. We note that time-domain electromagnetic simulators based on FDTD can calculate the broadband response of nanophotonic simultaneously, but frequency-domain methods employing the finite element method (FEM) or rigorous coupled-wave analysis (RCWA) require two simulations per frequency point to obtain a FoM gradient. Due to its outstanding computational efficiency, the adjoint method has been widely employed in various nanophotonic devices such as metalens [108, 109], beam deflectors [110, 111], and demultiplexers [112, 113]. Compared to other evolutionary algorithms, such as GA, the adjoint method exhibits superior efficiency in converging to the high-quality optima.

The adjoint method facilitates the design process and achieves superior efficiency. Recently, several studies on color routers have adopted the adjoint method, as evidenced by noteworthy works [41–45], showcasing its proof through outstanding performance in computational results. As shown in figure 6(a), an RGB-IR color router for sub-wavelength size pixels was demonstrated using the adjoint method, which theoretically achieves near-perfect color routing efficiencies far exceeding the devices built using the GA [43]. The color router's height is 2 $\mu$m, and its overall width is determined by multiplying the pixel pitch width (400 nm) by the number of colors. The grid cells within this device, each 10 nm $\times$ 10 nm in size, vary in dielectric constant between $Si_3N_4$ and $SiO_2$ to optimize for desired wavelengths. It means that there are enormous DoF (32 000 binary DoF) to be exploited, even in a relatively modestly sized device. The optimized design that makes these large DoF nearly binary allows the router to achieve over 99% efficiency in all RGB IR bands. Similarly, a subwavelength three-dimensional color router consisting of $TiO_2/SiO_2$ in a height of 2 $\mu$m and 320 nm of pixel pitch was proposed in a configuration of RGGB Bayer pattern with perfect peak color routing efficiency as shown in figure 6(b) [44]. We also note that its performance is broadband, polarization-independent, and robust over various angles. Based on the same design method, 6- and 9-spectrum color routers are designed while achieving ideal routing efficiency beyond RGB [45]. By dividing the visible light range into six bands with an FWHM of 48 nm, the subpixels of one spectrum were made 330 $\times$ 330 nm in size to focus the light. The color routing efficiency was over 0.99, demonstrating good performance with more channels and shorter ranges. Unlike before, the nine channels for the short-wave infrared range were divided into nine channels to create a 3 $\times$ 3 layout. Also, the color routing efficiency was over 0.98, showing that the maximum efficiency can be achieved even with different ranges of spectral imaging, and the performance surpassed the theoretical limit of absorptive filters by ninefold, demonstrating the power of spectral routers. These results represent the initial theoretical validation of a subwavelength device that unlocks the full potential of color routing. Using the adjoint method to design a metasurface-based color router extends the capabilities of wavelength-multiplexed silicon metasurfaces and demonstrates efficiencies that exceed current state-of-the-art methods [115]. A dielectric slab with a varying refractive index between air and polycrystalline silicon guides each design domain point in the iterative process. Through multiple iterations, each point's refractive index converges to air or polycrystalline silicon, resulting in a device that amalgamates the distinctive properties of both materials. The router

redirects five incident plane waves of different wavelengths into five unique diffraction orders, resulting in an average absolute device efficiency proportional to $\sqrt{5}$ both theoretically and experimentally. This performance is significantly better than state-of-the-art devices.

Although the adjoint variable method is highly efficient in the computation of FoM gradients, formulating the adjoint problem becomes increasingly difficult when the FoM function gets complicated. The formulation often cannot be explicitly defined in the standard simulation methods [116]. In this context, the automatic differentiation (AD) method, which utilizes AD libraries to train artificial neural networks, provides an alternative way to efficiently compute FoM gradients by removing the need for manual constructions of the adjoint problem [116]. Kim *et al* designed a free-form polarization-sensitive single layer color router with 600 nm pixel pitch employing the AD of RCWA as shown in figure 6(c) [46]. The fabricated device exhibited the measured color routing efficiencies of 42%, 52%, and 33% at wavelengths of 660 nm, 530 nm, and 455 nm, respectively. Recently, another approach, the direct differentiation (DD) method, has been introduced, which aims to solve the problem of large memory requirements in AD by directly differentiating the FDTD update equations by exploiting the time reversibility of Maxwell's equations [114]. The method is applicable to both open and closed systems and reduces the memory requirement by 98% compared to the AD method. Figure 6(d) shows the inverse design of a multifunctional nanophotonic device for a frequency domain system using DD. Through frequency domain optimization, they designed a $TiO_2$-based color router that separates light incident at two different wavelengths ($\lambda_1 = 488$ nm and $\lambda_2 = 633$ nm) into two separate spatial regions [114]. The optimized device was successfully designed to operate effectively at both wavelengths by maximizing the overall objective function and concurrently enhancing the minimum of the objective function for each wavelength, resulting in a clear Gaussian field profile for the transmitted electric field at the intended wavelengths.

Thus far, gradient-based approaches have shown efficient optimization of color routing devices. While these methods achieve near-perfect efficiency, the optimized devices include many free-form structures, which could be a significant challenge in the fabrication process. One can apply fabrication constraints to the existing optimization approach to overcome this limitation, simplifying the structure. The adjoint optimization starts with grayscale permittivities. Then, the grayscale permittivities gradually converge to the binary values through the penalization method [118] or density filters [119]. This naturally leads to a binary solution without sacrificing the optical efficiency of the optimized devices [120]. In this penalization process, one can also apply a conic filter, which enforces the optimized devices' aspect ratio or minimum length scale constraints. The filtering techniques are often applied in optimization algorithms to smooth out the design variables or the sensitivity distribution, making the optimization process more stable and helping to avoid local minima. The conic filter in adjoint optimization is a spatial filter applied to the gradient data, smoothing the data in a manner that reflects fabrication constraints. In figure 7(a), a 3D nanostructured design is depicted, optimizing the distribution of linearly polarized light into four individual focal planes based on the RGB spectral bands. The optimization process independently targets the polarization of R and B pixels, adhering to the 2D Bayer pattern [41]. Simultaneously, the design's diagonal mirror symmetry enables efficient sorting of orthogonal polarization, adding polarization selectivity specifically for G pixels [121]. This structure, designed for 3D printing [122], consists of a 2 $\mu$m $\times$ 2 $\mu$m $\times$ 2 $\mu$m cube composed of a polymer with a refractive index of 1.56 and air. The device's volume is discretized into a 100 $\times$ 100 $\times$ 100 grid, with each voxel measuring 20 nm $\times$ 20 nm $\times$ 20 nm. Despite optimizing the device only as a binary structure without setting restrictions on the minimum size, there are no structures smaller than three voxels in size. In contrast to figure 6(b), which enables color routing without a focal length, this device requires a focal length of 1.5 $\mu$m. R and B pixels exhibited routing efficiencies exceeding 90%, while G pixel achieved over 60%. However, implementing these devices into image sensors requires complicated fabrication processes. They might be realized through the multilayer lithography structure [123], constructing 3D devices by depositing 2D layers; however, the multilayer fabrication requires highly accurate alignment among the layers and demands high cost. Using a blurring filter to determine the minimum feature size, a layered design composed of $TiO_2$ and $SiO_2$ is created, a structure that can be fabricated with standard lithography. The device is scaled up to the centimeter range to validate the fabrication-constrained design experimentally. The scaled device operates within the microwave frequencies of the $K_a$ band, consisting of 20 sheets of polypropylene, each with a thickness of 1.6 mm and patterned with a minimum size of 1 mm. When illuminated by a Gaussian beam, the device's efficiency in scattering complex microwave fields showed similar results between simulation and experimental averages, both in the range of 40%.

Beyond the gradient-based optimization that incorporates fabrication constraints, shape optimization emerges as a viable method for generating designs that are more amenable to fabrication. This form of optimization refines the geometry of the structure by accurately calculating gradients relative to changes in the boundary, thereby potentially mitigating the propensity for fabrication inaccuracies characteristic of grid-based methods. Figure 7(b) shows a color router created from an optimally performing four-layer structure against one conceived from a fully three-dimensional structure [117]. This comparison evaluates the efficiency of eleven distinct configurations for each model through a comprehensive analysis of full-color correction efficiency. The optimization process for the router entails a sequence of adjustments ranging from fully solid to fully void, incorporating nine uniformly distributed index levels to refine the complexity inherent in each layer. The three-dimensional structure achieved a peak efficiency of 34%, which notably surpassed the color correction capability of traditional absorption filters by a factor of two, the latter typically exhibiting an efficiency of 17%. Although the

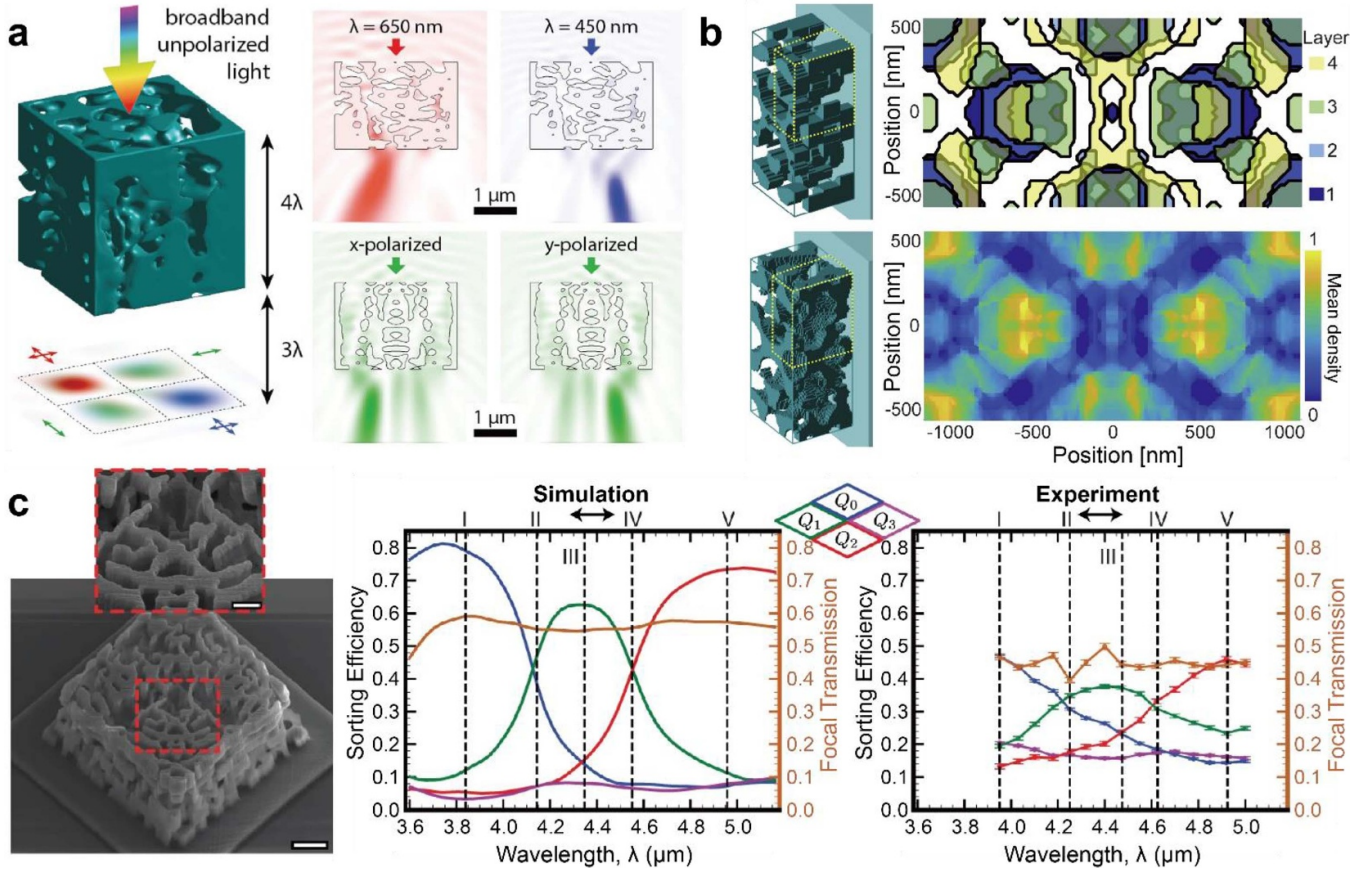


**Figure 7.** Free-form nanophotonic color routers designed based on adjoint methods with fabrication constraints. (a) 3D multifunctional volumetric color router and the field intensity profiles of RGB colors. Reproduced from [41]. CC BY 4.0. (b) A schematic of a four-layer RGB Bayer color router. Reproduced with permission from [117]. CC BY-NC-ND 4.0. (c) SEM images of a micrometer-scale free-form polarization-sensitive nanophotonic color router and showcasing simulation and experimental routing efficiencies. Reproduced from [42], with permission from Springer Nature.

four-layer configuration demonstrated marginally lower efficiency, it retained the advantage of compatibility with conventional photolithography techniques, offering a pragmatic balance between performance and manufacturability.

Implementing fabrication constraints, while concurrently enabling global explorations of the design space by the multilayer structure, fosters the development of processable nanophotonic structures. These enhancements in structure design augment the performance and adaptability of imaging systems. As illustrated in figure 7(c), the optimization process involves calculating the gradient of each layer within the multilayer structure as the mean gradient of all its vertical components, followed by their simultaneous optimization [42]. This method guarantees structural integrity and optimizes efficiency. The depicted device, as revealed in the SEM images, was manufactured using a two-photon polymerization 3D printer. This printer employs an IP-Dip polymer to fabricate a subwavelength color router, which exhibits minimal losses within the mid-infrared spectrum. During experimental procedures, the device was exposed to light from a quantum cascade laser, which operates within a constrained wavelength range of 3.95–5.05 $\mu$m. Consequently, the experimental results diverged from those anticipated by the full spectrum simulation. Under conditions of horizontal polarization illumination, the peak alignment efficiencies for the RGB bands were predicted to be 0.73, 0.63, and 0.78, respectively. The experimental findings, however, indicated efficiencies of 0.46, 0.38, and 0.47 for these bands. This investigation showcases the boundless potential of devices based on adjoint optimization in nanophotonics, evidenced by the creation of devices capable of classifying Stokes polarimetry and angular momentum, alongside a device for classifying linear polarization. Rather than tailoring each structure for a unique function, this research explores the feasibility of utilizing mechanical reconfiguration to adapt a single optimized structure for multiple functionalities. By applying rotational or shearing forces, a structure's geometry can be altered, enabling it to perform diverse optical tasks such as color routing, focusing, or polarization [124]. This multifaceted approach demonstrates the viability of employing adjoint optimization for the design of mechanically reconfigurable optical devices. It highlights the advantage of mechanically altering a device to bestow it with desired optical properties, thereby introducing a novel strategy for integrating optimization with mechanical versatility.

## 4. Outlook

We anticipate that nanophotonic color routers will soon be incorporated into commercial high-end CMOS image sensors with subwavelength pixels by replacing conventional MLA and absorptive color filters at least in part. This transition is inevitable as aggressive pixel downscaling approaches to diffraction limit and thus full-wave optic design and high optical efficiency become necessary. Although fixed-form devices showed some meaningful advancement in realizing color routing functionality, the free-form design approach may dominate the actual device implementation as it generally provides much higher performance by accessing vast design spaces that cannot be explored previously.

Although remarkable research progress has been made in this field, there still exist a number of challenges that need to be overcome. One of the biggest challenges is fabrication-compatible design. As we discussed in the previous sections, it is already demonstrated theoretically that the optical efficiency of a free-form color router can reach almost unity [43–45]. However, the proposed device structures are composed of a few tens to even a few hundreds of layers, and each layer is composed of $\sim 10^4$ voxels with 10 nm side lengths, which are practically challenging to create. Thus far, experimental verifications were performed by designing and fabricating single-layer structures, or by upscaling the entire device to the microwave to mid-infrared frequencies to avoid nanofabrication challenges. The most viable approach to create multi-layer color routers would be to generate multiple photomasks corresponding to each layer, fabricating each layer on top of each other in a sequential manner. The main problem in this process is the difficulty in aligning the layers. Moreover, repeating tens of EUV photolithography processes would make free-from color routers less favorable compared to conventional CMOS image sensors in the perspective of commercial cost-effectiveness. Although rapid recent advancements in nanopatterning techniques, such as 3D laser nanolithography with sub-wavelength resolution [122], would facilitate the fabrication of complex-shaped devices to some extent, it is necessary to come up with fabrication-conscious design methods for free-from color routers.

Securing fabrication compatibility is not as simple as just imposing a certain minimum feature size during the design optimization process. Numerically optimized free-from devices tend to be vulnerable to even a small structural perturbation, which is inevitable in device fabrication [59, 125]. Therefore, it is important to develop design optimization methods that produce devices with robustness against realistic fabrication errors [126, 127]. To be commercially meaningful, the optimization of color router design should also include techno-ecomnic analysis and thereby have the manufacturing cost in the objective function, which should affect the choice of the minimum feature size and the fabrication tolerance.

Another important issue of free-from color routers is a significant performance drop under oblique incidence. In most previous demonstrations, the optical efficiencies of color routers exhibited a strong dependence on incidence angle as the local phase difference for color routing is disrupted when the incident light becomes oblique [38–40]. Considering that the main application of CMOS image sensors is in smart phones and digital cameras, it is desirable that future color router designs maintain their performance under oblique incident light at angles up to 8° [91]. Lastly, we point out that the current nanophotonic color routers are prone to inter-pixel crosstalk, as they are designed based on electromagnetic simulation in the periodic pixel array with a delocalized plane wave with a single wavevector. In this design scheme, the light may propagate to nearby unit pixels rather than those directly in front, which hinders the clarity of high-resolution images. Therefore, an elaborate design approach to suppress the inter-pixel crosstalk must be developed. By overcoming these ongoing challenges, nanophotonic color routers will emerge as an essential building block of subwavelength pixelated CMOS image sensors.

## Data availability statement

No new data were created or analysed in this study.

## Acknowledgments

This research was supported by the Ministry of Trade, Industry & Energy (MOTIE) (1415180303) and the Korea Semiconductor Research Consortium (KSRC) (20019357). This work was also supported by the National Research Foundation of Korea (NRF) grant funded by the Korea government (MSIT) (NRF-2022K1A3A1A91093776, NRF-2022R1A2C2092095).

## ORCID iDs

Sangbin Lee https://orcid.org/0009-0009-2563-3764
Jiwon Kang https://orcid.org/0000-0003-2414-6963
Haejun Chung https://orcid.org/0000-0001-8959-237X
Min Seok Jang https://orcid.org/0000-0002-5683-1925

## References

[1] Kita D M, Miranda B, Favela D, Bono D, Michon J, Lin H, Gu T and Hu J 2018 High-performance and scalable on-chip digital Fourier transform spectroscopy *Nat. Commun.* **9** 4405
[2] Wang Z *et al* 2019 Single-shot on-chip spectral sensors based on photonic crystal slabs *Nat. Commun.* **10** 1020
[3] Yesilkoy F, Arvelo E R, Jahani Y, Liu M, Tittl A, Cevher V, Kivshar Y and Altug H 2019 Ultrasensitive hyperspectral imaging and biodetection enabled by dielectric metasurfaces *Nat. Photon.* **13** 390–6
[4] Yako M, Yamaoka Y, Kiyohara T, Hosokawa C, Noda A, Tack K, Spooren N, Hirasawa T and Ishikawa A 2023 Video-rate hyperspectral camera based on a CMOS-compatible random array of Fabry-Perot filters *Nat. Photon.* **17** 218–223
[5] Ishikawa M, Ogawa K, Komuro T and Ishii I 1999 *A* CMOS vision chip with SIMD processing element array for 1 ms image processing *1999 IEEE Int. Solid-State Circuits Conf.. Digest of Technical Papers. ISSCC* 1st edn

[6] Hsu T H, Chen Y R, Liu R S, Lo C C, Tang K T, Chang M F and Hsieh C C 2021 A 0.5-V real-time computational CMOS image sensor with programmable kernel for feature extraction *IEEE J. Solid-State Circuits* **56** 1588–96

[7] Bigas M, Cabruja E, Forest J and Salvi J 2006 Review of CMOS image sensors *Microelectron. J.* **37** 433–51

[8] El Gamal A and Eltoukhy H 2005 CMOS image sensors *IEEE Circuits Devices Mag.* **21** 6–20

[9] Lulé T, Benthien S, Keller H, Mütze F, Rieve P, Seibel K, Sommer M and Böhm M 2000 Sensitivity of CMOS based imagers and scaling perspectives *IEEE Trans. Electron Devices* **47** 2110–22

[10] Sukegawa S, Umebayashi T, Nakajima T, Kawanobe H, Koseki K, Hirota I, Haruta T, Kasai M, Fukumoto K and Wakano T 2013 A 1/4-inch 8Mpixel back-illuminated stacked CMOS image sensor *2013 IEEE Int. Solid-State Circuits Conf. Digest of Technical Papers* (IEEE)

[11] Rung R, Momose H and Nagakubo Y 1982 Deep trench isolated CMOS devices *1982 Int. Electron Devices Meeting* (IEEE)

[12] Lee G-D R, Kim D-H, Kwon D, Park J-E, Cho D, Kang J, Park G, Kang J, Jang M and Oh S 2023 A 0.5 $\mu$m pixel 3-layer stacked CMOS image sensor with deep contact and in-pixel Cu-Cu bonding technology *2023 Int. Electron Devices Meeting (IEDM)* (IEEE)

[13] Zheludev N I and Yuan G H 2022 Optical superoscillation technologies beyond the diffraction limit *Nat. Rev. Phys.* **4** 16–32

[14] Chen M K, Wu Y F, Feng L, Fan Q B, Lu M H, Xu T and Tsai D P 2021 Principles, functions, and applications of optical meta-lens *Adv. Opt. Mater.* **9** 2001414

[15] Yuan W, Li L H, Lee W B and Chan C Y 2018 Fabrication of microlens array and its application: a review *Chin. J. Mech. Eng.* **31** 1–9

[16] Chung H J, Zhou Z G and Bermel P 2017 Collimated thermal radiation transfer via half Maxwell's fish-eye lens for thermophotovoltaics *Appl. Phys. Lett.* **110** 201111

[17] Khorasaninejad M, Chen W T, Devlin R C, Oh J, Zhu A Y and Capasso F 2016 Metalenses at visible wavelengths: diffraction-limited focusing and subwavelength resolution imaging *Science* **352** 1190–4

[18] Wang Y J *et al* 2021 High-efficiency broadband achromatic metalens for near-IR biological imaging window *Nat. Commun.* **12** 5560

[19] Chen W T, Zhu A D Y and Capasso F 2020 Flat optics with dispersion-engineered metasurfaces *Nat. Rev. Mater.* **5** 604–20

[20] Vashistha V, Vaidya G, Hegde R S, Serebryannikov A E, Bonod N and Krawczyk M 2017 All-dielectric metasurfaces based on cross-shaped resonators for color pixels with extended gamut *ACS Photonics* **4** 1076–82

[21] Liu Z, Zhu D, Rodrigues S P, Lee K-T and Cai W 2018 Generative model for the inverse design of metasurfaces *Nano Lett.* **18** 6570–6

[22] Shi X, Qiu T, Wang J, Zhao X and Qu S 2020 Metasurface inverse design using machine learning approaches *J. Phys. D: Appl. Phys.* **53** 275105

[23] Park J, Kim S, Nam D W, Chung H, Park C Y and Jang M S 2022 Free-form optimization of nanophotonic devices: from classical methods to deep learning *Nanophotonics* **11** 1809–45

[24] Holland J H 1992 Genetic algorithms *Sci. Am.* **267** 66–72

[25] Jafar-Zanjani S, Inampudi S and Mosallaei H 2018 Adaptive genetic algorithm for optical metasurfaces design *Sci. Rep.* **8** 11040

[26] Park J, Kim S, Lee J, Menabde S G and Jang M S 2019 Ultimate light trapping in a free-form plasmonic waveguide *Phys. Rev. Appl.* **12** 024030

[27] Giles M B, Pierce N A, Ventruba P, Kucera M and Kachlík P 2000 An introduction to the adjoint approach to design *Flow Turbulence Combust.* **65** 393–415

[28] Li Z, Pestourie R, Park J-S, Huang Y-W, Johnson S G and Capasso F 2022 Inverse design enables large-scale high-performance meta-optics reshaping virtual reality *Nat. Commun.* **13** 2409

[29] Chung H and Miller O D 2020 Tunable metasurface inverse design for 80% switching efficiencies and 144° angular deflection *ACS Photonics* **7** 2236–43

[30] Zou X J, Lin R Y, Fu Y L, Gong G X, Zhou X X, Wang S M, Zhu S N and Wang Z L 2024 Advanced optical imaging based on metasurfaces *Adv. Opt. Mater.* **12** 2203149

[31] Yao J, Lin R, Chen M K and Tsai D P 2023 Integrated-resonant metadevices: a review *Adv. Photon.* **5** 024001

[32] Chen Q, Nan X H, Chen M J, Pan D H, Yang X G and Wen L 2021 Nanophotonic color routing *Adv. Mater.* **33** 2103815

[33] Miyata M, Nakajima M and Hashimoto T 2019 High-sensitivity color imaging using pixel-scale color splitters based on dielectric metasurfaces *ACS Photonics* **6** 1442–50

[34] Shao Y F, Guo S H, Chen R, Dang Y D, Zhou Y, Wang Y B, Zhan J J, Yu J Q, Ju B-F and Ma Y G 2023 Pixelated NIR-VIS spectral routers based on 2D mie-type metagratings *Laser Photon. Rev.* **17** 2300027

[35] Chen B H *et al* 2017 GaN metalens for pixel-level full-color routing at visible light *Nano Lett.* **17** 6345–52

[36] Miyata M, Nemoto N, Shikama K, Kobayashi F and Hashimoto T 2021 Full-color-sorting metalenses for high-sensitivity image sensors *Optica* **8** 1596–604

[37] Chen M J, Wen L, Pan D H, Cumming D R S, Yang X G and Chen Q 2021 Full-color nanorouter for high-resolution imaging *Nanoscale* **13** 13024–9

[38] Zou X J, Zhang Y M, Lin R Y, Gong G X, Wang S M, Zhu S N and Wang Z L 2022 Pixel-level Bayer-type colour router based on metasurfaces *Nat. Commun.* **13** 3288

[39] Li J H *et al* 2022 Single-layer Bayer metasurface via inverse design *ACS Photonics* **9** 2607–13

[40] Kim S, Park C, Kim S, Chung H and Jang M S 2023 Design parameters of free-form color splitters for subwavelength pixelated image sensors *Iscience* **26** 107788

[41] Camayd-Muñoz P, Ballew C, Roberts G and Faraon A 2020 Multifunctional volumetric meta-optics for color and polarization image sensors *Optica* **7** 280–3

[42] Roberts G, Ballew C, Zheng T Z, Garcia J C, Camayd-Muñoz S, Hon P W C and Faraon A 2023 3D-patterned inverse-designed mid-infrared metaoptics *Nat. Commun.* **14** 2768

[43] Zhao N, Catrysse P B and Fan S H 2021 Perfect RGB-IR color routers for sub-wavelength size CMOS image sensor pixels *Adv. Photon. Res.* **2** 2000048

[44] Catrysse P B, Zhao N, Jin W L and Fan S H 2022 Subwavelength Bayer RGB color routers with perfect optical efficiency *Nanophotonics* **11** 2381–7

[45] Catrysse P B and Fan S H 2023 Spectral routers for snapshot multispectral imaging *Appl. Phys. Lett.* **123** 261105

[46] Kim C, Hong J, Jang J, Lee G Y, Kim Y, Jeong Y and Lee B 2024 Freeform metasurface color router for deep submicron pixel image sensors *Sci. Adv.* **10** eadn9000

[47] Yokogawa S, Burgos S P and Atwater H A 2012 Plasmonic color filters for CMOS image sensor applications *Nano Lett.* **12** 4349–54

[48] Berzins J, Fasold S, Pertsch T, Bäumer S M B and Setzpfandt F 2019 Submicrometer nanostructure-based RGB filters for CMOS image sensors *ACS Photonics* **6** 1018

[49] Shegai T, Chen S, Miljkovic V D, Zengin G, Johansson P and Käll M 2011 A bimetallic nanoantenna for directional colour routing *Nat. Commun.* **2** 481

[50] Vercruysse D, Sonnefraud Y, Verellen N, Fuchs F B, Di Martino G, Lagae L, Moshchalkov V V, Maier S A and Van Dorpe P 2013 Unidirectional side scattering of light by a single-element nanoantenna *Nano Lett.* **13** 3843–9

[51] Nishiwaki S, Nakamura T, Hiramoto M, Fujii T and Suzuki M 2013 Efficient colour splitters for high-pixel-density image sensors *Nat. Photon.* **7** 240–6

[52] Yan C, Yang K Y and Martin O J F 2017 Fano-resonance-assisted metasurface for color routing *Light-Sci. Appl.* **6** e17017

[53] Maier S A 2007 *Plasmonics: Fundamentals and Applications* vol 1 (Springer)

[54] Zhuo X L, Yip H K, Cui X M, Wang J F and Lin H Q 2019 Colour routing with single silver nanorods *Light-Sci. Appl.* **8** 39

[55] Li J Q, Verellen N, Vercruysse D, Bearda T, Lagae L and Van Dorpe P 2016 All-dielectric antenna wavelength router with bidirectional scattering of visible light *Nano Lett.* **16** 4396–403

[56] Kim S J, Kang J H, Mutlu M, Park J, Park W, Goodson K E, Sinclair R, Fan S H, Kik P G and Brongersma M L 2018 Anti-Hermitian photodetector facilitating efficient subwavelength photon sorting *Nat. Commun.* **9** 316

[57] Barber P and Yeh C 1975 Scattering of electromagnetic waves by arbitrarily shaped dielectric bodies *Appl. Opt.* **14** 2864–72

[58] Genevet P, Capasso F, Aieta F, Khorasaninejad M and Devlin R 2017 Recent advances in planar optics: from plasmonic to dielectric metasurfaces *Optica* **4** 139–52

[59] Seo D, Nam D W, Park J, Park C Y and Jang M S 2022 Structural optimization of a one-dimensional freeform metagrating deflector via deep reinforcement learning *ACS Photonics* **9** 452–8

[60] Park C, Kim S, Jung A W, Park J, Seo D, Kim Y, Park C, Park C Y and Jang M S 2024 Sample-efficient inverse design of freeform nanophotonic devices with physics-informed reinforcement learning *Nanophotonics* **13** 1483–92

[61] Wang L, Kruk S, Koshelev K, Kravohenk I, Luther-Davies B and Kivshar Y 2018 Nonlinear wavefront control with all-dielectric metasurfaces *Nano Lett.* **18** 3978–84

[62] Chen X Z, Huang L L, Mühlenbernd H, Li G X, Bai B F, Tan Q F, Jin G F, Qiu C W, Zhang S and Zentgraf T 2012 Dual-polarity plasmonic metalens for visible light *Nat. Commun.* **3** 1198

[63] Wang S M *et al* 2018 A broadband achromatic metalens in the visible *Nat. Nanotechnol.* **13** 227–32

[64] Chen W T, Zhu A Y, Sanjeev V, Khorasaninejad M, Shi Z J, Lee E and Capasso F 2018 A broadband achromatic metalens for focusing and imaging in the visible *Nat. Nanotechnol.* **13** 220

[65] Heiden J T and Jang M S 2022 Design framework for polarization-insensitive multifunctional achromatic metalenses *Nanophotonics* **11** 583–91

[66] Yu N F, Aieta F, Genevet P, Kats M A, Gaburro Z and Capasso F 2012 A broadband, background-free quarter-wave plate based on plasmonic metasurfaces *Nano Lett.* **12** 6328–33

[67] Cong L Q, Xu N N, Gu J Q, Singh R, Han J G and Zhang W L 2014 Highly flexible broadband terahertz metamaterial quarter-wave plate *Laser Photon. Rev.* **8** 626–32

[68] Huang L L *et al* 2013 Three-dimensional optical holography using a plasmonic metasurface *Nat. Commun.* **4** 2808

[69] Ni X J, Kildishev A V and Shalaev V M 2013 Metasurface holograms for visible light *Nat. Commun.* **4** 2807

[70] Zheng G, Mühlenbernd H, Kenney M, Li G, Zentgraf T and Zhang S 2015 Metasurface holograms reaching 80% efficiency *Nat. Nanotechnol.* **10** 308–12

[71] Zou X J, Lin R Y, Fu Y L, Gong G X, Zhou X X, Wang S M, Zhu S N and Wang Z L 2023 Advanced optical imaging based on metasurfaces *Adv. Opt. Mater.* **12** 2203149

[72] Kerker M, Wang D S and Giles C L 1983 Electromagnetic scattering by magnetic spheres *J. Opt. Soc. Am.* **73** 765–7

[73] Liu W and Kivshar Y S 2018 Generalized Kerker effects in nanophotonics and meta-optics [Invited] *Opt. Express* **26** 13085–105

[74] Babicheva V E and Evlyukhin A B 2017 Resonant lattice Kerker effect in metasurfaces with electric and magnetic optical responses *Laser Photon. Rev.* **11** 1700132

[75] Yan J H, Zhu D Y, Bao Y J, Chen Q, Li B J and Cai W S 2024 Design of multifunctional color routers with Kerker switching using generative adversarial networks *Laser Photon. Rev.* **18** 2300592

[76] Pancharatnam S 1956 Generalized theory of interference, and its applications: part I. Coherent pencils *Proc. Indian Acad. Sci.* A **44** 247–62

[77] Luo W, Sun S, Xu H-X, He Q and Zhou L 2017 Transmissive ultrathin Pancharatnam-Berry metasurfaces with nearly 100% efficiency *Phys. Rev. Appl.* **7** 044033

[78] Ding X, Monticone F, Zhang K, Zhang L, Gao D, Burokur S N, De Lustrac A, Wu Q, Qiu C W and Alù A 2015 Ultrathin Pancharatnam–Berry metasurface with maximal cross-polarization efficiency *Adv. Mater.* **27** 1195–200

[79] Lin D M, Holsteen A L, Maguid E, Wetzstein G, Kik P G, Hasman E and Brongersma M L 2016 Photonic multitasking interleaved Si nanoantenna phased array *Nano Lett.* **16** 7671–6

[80] Maguid E, Yulevich I, Yannai M, Kleiner V, Brongersma M L and Hasman E 2017 Multifunctional interleaved geometric-phase dielectric metasurfaces *Light-Sci. Appl.* **6** e17027

[81] Khorasaninejad M, Ambrosio A, Kanhaiya P and Capasso F 2016 Broadband and chiral binary dielectric meta-holograms *Sci. Adv.* **2** e1501258

[82] Khorasaninejad M, Chen W T, Zhu A Y, Oh J, Devlin R C, Rousso D and Capasso F 2016 Multispectral chiral imaging with a metalens *Nano Lett.* **16** 4595–600

[83] Zang X F *et al* 2018 Polarization encoded color image embedded in a dielectric metasurface *Adv. Mater.* **30** 1707499

[84] Guo L H, Hu Z L, Wan R Q, Long L Y, Li T, Yan J C, Lin Y, Zhang L, Zhu W H and Wang L C 2019 Design of aluminum nitride metalens for broadband ultraviolet incidence routing *Nanophotonics* **8** 171–80

[85] Kim C, Hong J and Lee B 2021 Visible color routing metasurface using dual focal phase profile in green light. in Holography, Diffractive Optics, and Applications XI *Proc. SPIE* **11898** 224–8

[86] Zhong R X, Xu X Y, Zhou Y L, Liang H W and Li J T 2023 High-efficiency integrated color routers by simple identical nanostructures for visible and near-infrared wavelengths *Photonics* **10** 536

[87] Hong Y J, Jeon B J, Ki Y G and Kim S J 2024 A metasurface color router facilitating RGB-NIR sensing for an image sensor application *Nanophotonics* **13** 1407–15

[88] Mansouree M, Kwon H, Arbabi E, McClung A, Faraon A and Arbabi A 2020 Multifunctional 2.5D metastructures enabled by adjoint optimization *Optica* **7** 77–84

[89] Zhou Y, Kravchenko I I, Wang H, Nolen J R, Gu G and Valentine J 2018 Multilayer noninteracting dielectric metasurfaces for multiwavelength metaoptics *Nano Lett.* **18** 7529–37

[90] Yun S, Roh S, Lee S, Park H, Lim M, Ahn S and Choo H 2021 Highly efficient color separation and focusing in the sub-micron CMOS image sensor *2021 IEEE Int. Electron Devices Meeting (IEDM)*

[91] Choi C, Park J, Lee Y, Kim B, Kim J, Kim S, Kim J, Roh S, Ahn S and Mun S 2023 Optical design of dispersive metasurface nano-prism structure for high sensitivity CMOS image sensor *2023 Int. Electron Devices Meeting (IEDM)* (IEEE)

[92] Ade P A, Aghanim N, Arnaud M, Ashdown M, Aumont J, Baccigalupi C, Banday A, Barreiro R, Bartlett J and Bartolo N 2016 Planck 2015 results-xiii. cosmological parameters *Astron. Astrophys.* **594** A13

[93] Kim S, Shin J M, Lee J, Park C, Lee S, Park J, Seo D, Park S, Park C Y and Jang M S 2021 Inverse design of organic light-emitting diode structure based on deep neural networks *Nanophotonics* **10** 4533–41

[94] Katoch S, Chauhan S S and Kumar V 2021 A review on genetic algorithm: past, present, and future *Multimedia Tools Appl.* **80** 8091–126

[95] Shimodaira H 1996 A new genetic algorithm using large mutation rates and population-elitist selection (GALME) *Eighth IEEE Int. Conf. on Tools with Artificial Intelligence, Proc.* pp 25–32

[96] Weile D S, Michielssen E and Goldberg D E 1996 Genetic algorithm design of Pareto optimal broadband microwave absorbers *IEEE Trans. Electromagn. Compat.* **38** 518–25

[97] Cai H Y, Sun Y, Wang X P and Zhan S Y 2020 Design of an ultra-broadband near-perfect bilayer grating metamaterial absorber based on genetic algorithm *Opt. Express* **28** 15347–59

[98] Michielssen E, Sajer J M, Ranjithan S and Mittra R 1993 Design of lightweight, broad-band microwave absorbers using genetic algorithms *IEEE Trans. Microwave Theory Tech.* **41** 1024–31

[99] Lin C H, Chen Y S, Lin J T, Wu H C, Kuo H T, Lin C F, Chen P and Wu P C 2021 Automatic inverse design of high-performance beam-steering metasurfaces via genetic-type tree optimization *Nano Lett.* **21** 4981–9

[100] Xu D, Luo Y, Luo J, Pu M B, Zhang Y X, Ha Y L and Luo X G 2021 Efficient design of a dielectric metasurface with transfer learning and genetic algorithm *Opt. Mater. Express* **11** 1852–62

[101] Fan Y L, Xu Y K, Qiu M, Jin W, Zhang L, Lam E Y, Tsai D P and Lei D Y 2020 Phase-controlled metasurface design via optimized genetic algorithm *Nanophotonics* **9** 3931–9

[102] Cai H G, Srinivasan S, Czaplewski D A, Martinson A B F, Gosztola D J, Stan L, Loeffler T, Sankaranarayanan S K R S and López D 2020 Inverse design of metasurfaces with non-local interactions *npj Comput. Mater.* **6** 116

[103] Zou X J, Gong G X, Lin Y, Fu B Y, Wang S M, Zhu S N and Wang Z L 2023 Metasurface-based polarization color routers *Opt. Lasers Eng.* **163** 107472

[104] Peng Y Q, Lu H P, Zhang D S, Wang L C, Ma Z Y and Xiao J J 2023 Inverse design of a light nanorouter for a spatially multiplexed optical filter *Opt. Lett.* **48** 6232–5

[105] Miller O D 2012 *Photonic Design: From Fundamental Solar Cell Physics to Computational Inverse Design* (University of California)

[106] Tijhuis A G, Belkebir K, Litman A C S and de Hon B P 2001 Theoretical and computational aspects of 2-D inverse profiling *IEEE Trans. Geosci. Remote Sens.* **39** 1316–30

[107] Altman C and Suchy K 2011 *Reciprocity, Spatial Mapping and Time Reversal in Electromagnetics* (Springer Science & Business Media)

[108] Chung H and Miller O D 2020 High-NA achromatic metalenses by inverse design *Opt. Express* **28** 6945–65

[109] Mansouree M, McClung A, Samudrala S and Arbabi A 2021 Large-scale parametrized metasurface design using adjoint optimization *ACS Photonics* **8** 455–63

[110] Sell D, Yang J J, Doshay S, Yang R and Fan J A 2017 Large-angle, multifunctional metagratings based on freeform multimode geometries *Nano Lett.* **17** 3752–7

[111] Callewaert F, Velev V, Kumar P, Sahakian A V and Aydin K 2018 Inverse-designed broadband all-dielectric electromagnetic metadevices *Sci. Rep.* **8** 1358

[112] Piggott A Y, Lu J, Lagoudakis K G, Petykiewicz J, Babinec T M and Vuckovic J 2015 Inverse design and demonstration of a compact and broadband on-chip wavelength demultiplexer *Nat. Photon.* **9** 374

[113] Wang K Y, Ren X S, Chang W J, Lu L H, Liu D M and Zhang M M 2020 Inverse design of digital nanophotonic devices using the adjoint method *Photon. Res.* **8** 528–33

[114] Tang R J, Lim S W D, Ossiander M, Yin X H and Capasso F 2023 Time reversal differentiation of FDTD for photonic inverse design *ACS Photonics* **10** 4140–50

[115] Sell D, Yang J J, Doshay S and Fan J A 2017 Periodic dielectric metasurfaces with high-efficiency, multiwavelength functionalities *Adv. Opt. Mater.* **5** 1700645

[116] Minkov M, Williamson I A D, Andreani L C, Gerace D, Lou B C, Song A Y, Hughes T W and Fan S H 2020 Inverse design of photonic crystals through automatic differentiation *ACS Photonics* **7** 1729–41

[117] Johlin E 2021 Nanophotonic color splitters for high-efficiency imaging *Iscience* **24** 102268

[118] Giannakoglou K C and Papadimitriou D I 2008 Adjoint methods for shape optimization *Optimization and Computational Fluid Dynamics* (Springer) pp 79–108

[119] Svanberg K and Svärd H 2013 Density filters for topology optimization based on the pythagorean means *Struct. Multidiscipl. Optim.* **48** 859–75

[120] Ballew C, Roberts G, Zheng T Z and Faraon A 2023 Constraining continuous topology optimizations to discrete solutions for photonic applications *ACS Photonics* **10** 836–44

[121] Ahn S, Catrysse P B, Mun S, Cho C, Lim M, Roh S, Yun S and Fan S 2023 Polarization independent freeform color router for subwavelength-pixel CMOS image sensors. in high contrast metastructures XII *Proc. SPIE* **PC12432** PC124320A

[122] Zhou X Q, Hou Y H and Lin J Q 2015 A review on the processing accuracy of two-photon polymerization *AIP Adv.* **5** 030701

[123] Sherwood-Droz N and Lipson M 2011 Scalable 3D dense integration of photonics on bulk silicon *Opt. Express* **19** 17758–65

[124] Ballew C, Roberts G, Camayd-Muñoz S, Debbas M F and Faraon A 2021 Mechanically reconfigurable multi-functional meta-optics studied at microwave frequencies *Sci. Rep.* **11** 11145

[125] Gostimirovic D, Grinberg Y, Xu D X and Liboiron-Ladouceur O 2023 Improving fabrication fidelity of integrated nanophotonic devices using deep learning *ACS Photonics* **10** 1953–61

[126] Wang F W, Jensen J S and Sigmund O 2011 Robust topology optimization of photonic crystal waveguides with tailored dispersion properties *J. Opt. Soc. Am.* B **28** 387–97

[127] Wen F F, Jiang J Q and Fan J A 2020 Robust freeform metasurface design based on progressively growing generative networks *ACS Photonics* **7** 2098–104